Spectromicroscopy and coherent diffraction imaging: focus on energy materials applications

Adam P. Hitchcock and Michael F. Toney

Crystallography Journals Online is available from **journals.iucr.org**

Spectromicroscopy and coherent diffraction imaging: focus on energy materials applications

Adam P. Hitchcock[a]* and Michael F. Toney[b]*

[a]Brockhouse Institute for Materials Research, McMaster University, Hamilton, Ontario, Canada L8S 4M1, and [b]SSRL, 2575 Sand Hill Road, Menlo Park, CA 94025, USA. *E-mail: aph@mcmaster.ca, mftoney@slac.stanford.edu

Current and future capabilities of X-ray spectromicroscopy are discussed based on coherence-limited imaging methods which will benefit from the dramatic increase in brightness expected from a diffraction-limited storage ring (DLSR). The methods discussed include advanced coherent diffraction techniques and nanoprobe-based real-space imaging using Fresnel zone plates or other diffractive optics whose performance is affected by the degree of coherence. The capabilities of current systems, improvements which can be expected, and some of the important scientific themes which will be impacted are described, with focus on energy materials applications. Potential performance improvements of these techniques based on anticipated DLSR performance are estimated. Several examples of energy sciences research problems which are out of reach of current instrumentation, but which might be solved with the enhanced DLSR performance, are discussed.

1. Introduction

When third-generation light sources first became available in the early 1990s, evolutionary improvements (better energy resolution, improved stability) dominated the ways in which they were used. It took the better part of a decade for researchers, who were used to second-generation sources, to fully understand and exploit the benefits of the higher brightness and orbit stability of third-generation rings. For example, techniques such as resonant scattering (Nugent, 2010; Fink *et al.*, 2013; Ade & Hitchcock, 2008), zone-plate-based scanning transmission X-ray microscopy (STXM) (Ade & Hitchcock, 2008; Howells *et al.*, 2007; Hitchcock, 2012) and coherent diffraction imaging (Quiney, 2010; Falcone *et al.*, 2011; Thibault *et al.*, 2008, 2014), all of which explicitly exploit the improved coherence and collimation properties of third-generation sources, took most of a decade to evolve. In terms of enhanced brightness, the step from current third-generation rings to the coming diffraction-limited storage rings (DLSRs) such as NSLS-II, MAX IV and Sirius, is as large as that between second- and third-generation storage rings. Thus there will be significant new opportunities and the transition will be facilitated by a consideration of the changes in source properties that a DLSR will bring (dealt with elsewhere in this issue) and their impact on present instrumentation, techniques and applications. In this article these factors are discussed for the case of real-space and coherent diffraction imaging with an emphasis on areas involving materials and processes for sustainable energy generation, storage, transformation and use. Recently there has been a large focus on energy materials research using third-generation facilities, including fundamental studies, post-mortem, *in situ* and *operando* approaches. Given the importance of this research to society and to the future of humanity, as well as the substantial base that current work provides to build enhanced and new methods for energy-related research using DLSRs, it is reasonable to expect DLSRs to have significant impact in the area of energy materials research.

Limiting the carbon-dioxide-induced temperature rise (*i.e.* global climate change) is currently one of humanity's greatest challenges. There are a number of approaches that are needed for developing a sustainable, carbon-neutral energy infrastructure (Muradov & Veziroğlu, 2012) but these require that we dramatically improve existing technologies, both in terms of performance and cost, largely by developing new Earth-abundant functional materials. This is true for energy generation (absorbers and transparent conductors), storage (anodes, cathodes, electrolytes), utilization (catalysts, membranes) and efficiency ('smart' window coatings). Electric vehicles require the on-board storage of large amounts of energy for a long cruising range. Sustainable energy generation using wind and solar is intermittent requiring large storage capabilities to balance supply and demand ('grid level' or stationary storage). Owing to their high energy density,

batteries offer the best technology for portable storage and are a contender for grid-level storage. However, existing technologies lack adequate energy storage capacity, have relatively short lifetimes, are expensive and are potentially unsafe. For energy transformation, hydrogen-burning polymer-electrolyte-membrane fuel cells promise to eliminate the use of fossil fuels for transportation (Debe, 2012; Maiya-lagan & Pasupathi, 2010), but they rely on expensive precious metal catalysts and have limited durability. Furthermore, the membranes are expensive and they cannot be used at the higher temperatures that would make catalysts more efficient. For solar and other applications, transparent conductors are needed, but the widely used indium-tin-oxide (ITO) is expensive and indium is rare, possibly creating a supply constraint. In these cases, existing materials limitations drive research for better performing, but inexpensive, functional materials.

This article emphasizes real-space X-ray spectromicroscopy and coherent-scattering imaging methods with emphasis on X-ray applications to energy materials and systems. Inevitably, some aspects overlap other articles in this special DLSR issue, including those on coherent imaging (ptychography) by Thibault *et al.* (2014), hard X-ray scanning microscopy by Schroer & Falkenberg (2014), fluorescence tomography of biological specimens by de Jonge *et al.* (2014) and X-ray spectroscopy for chemical and energy sciences by Frenkel & van Bokhoven (2014). We will describe how DLSRs can contribute to solving some of the materials problems described above, focusing on X-ray spectromicroscopy and reciprocal-space imaging. We then give some examples of currently impossible experiments that might be enabled by the DLSR and would have a huge impact on understanding sustainable energy materials.

2. Methods: exemplified by current capabilities

Fig. 1 outlines technologies currently used for X-ray imaging. This figure has been adapted from a review of methods for X-ray imaging and nanotomography (Withers, 2007). Improved spatial resolution and improved ability to follow dynamics on time scales of the order of microseconds or slower are likely the most dramatic consequences of performing these techniques on a DLSR. Improvements in signal quality due to more stable source properties will also be very important. Given that improved coherence will be one of the largest gains with DLSRs, we start by describing the capabilities of present-day coherence-limited instrumentation as a way of identifying areas of improvement. In real-space imaging, the methods which rely on the coherent fraction of present sources are those based on point probe methods where the focused X-rays are generated using Fresnel (Ade & Hitchcock, 2008; Howells *et al.*, 2007; Hitchcock, 2012), Bragg–Fresnel (Li *et al.*, 2003), multi-layer Laue (MLL) (Kang *et al.*, 2006; Yan *et al.*, 2013) lenses or combinations of these optical elements with reflective optics (Döring *et al.*, 2013). NSLS-II will have an emittance below 1 nm rad which is significantly better than existing third-generation synchrotron radiation
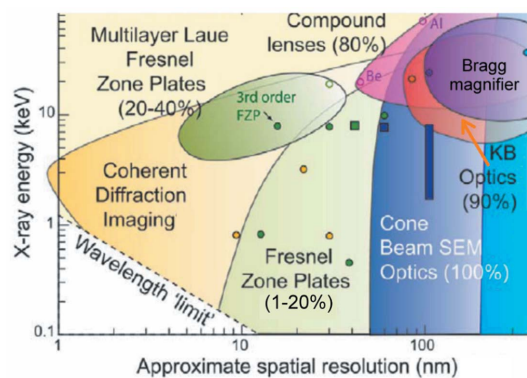

Figure 1
Classification of X-ray imaging instrumentation based on focusing technologies, achievable spatial resolution and photon energy range. Points indicate the current capabilities, while the coloured zones indicate the range of spatial resolution and photon energy where the technique is applicable, as well as the expected ultimate spatial resolution in a DLSR. Calculated resolutions are shown with open symbols, measured ones with filled symbols of the appropriate colour, circles correspond to synchrotrons and squares to laboratory sources. See the original article (Thibault *et al.*, 2014) for the sources of the specific performance data [adapted from Thibault *et al.* (2014), used with permission from *Materials Today* via RightsLink license 2517731089158].

sources, and thus a good marker for the transition to DLSR performance. The Hard X-ray Nanoprobe (HXN) beamline at NSLS-II has a target of achieving a 1 nm spot size. This will be realised through crossed MLL lenses which have already demonstrated sub-30 nm imaging at 12 keV in real-space imaging (Kang *et al.*, 2006), and 11 nm resolution in a ptychography verification (Huang *et al.*, 2014). MLL focused X-rays have been applied to phase imaging studies of solid oxide fuel cell cathodes (Yan *et al.*, 2013), providing information that was not obtainable by imaging using absorption or fluorescence detection. Perhaps more than any other, the 1 nm target set for the HXN beamline at NSLS-II exemplifies the explicit recognition of the advantages that DLSR will bring to imaging. For samples which are sufficiently radiation stable, it will provide both elemental sensitivity and the ability to fully define chemical states through detailed high-spectral-resolution X-ray absorption, and other spectroscopies.

Fig. 2(*a*) presents a cartoon of the Fresnel zone plate based instruments used for X-ray imaging of bulk (STXM) and surface (scanning photoelectron microscopy, SPEM) samples. In STXM, images are obtained serially by detecting the transmitted X-ray intensity while mechanically raster scanning the sample though the focal point of a zone plate (ZP) X-ray lens [or (in a few cases) by scanning the ZP and order-sorting aperture synchronously while the sample is stationary]. In SPEM, the same approach is applied except that the sample is usually X-ray opaque and the signal is detected by measuring energy-resolved photoelectrons using an electron energy analyzer, typically equipped with a multi-energy detection system (Guenther *et al.*, 2002). At present, the record spatial resolution for focusing using ZPs in a soft X-ray microscope is 10 nm (Chao *et al.*, 2012), although there are ambiguities in defining resolution in this context. For measurements at the C $1s$ edge ($h\nu \simeq 300$ eV, $\lambda \simeq 4$ nm) this is only a few times larger
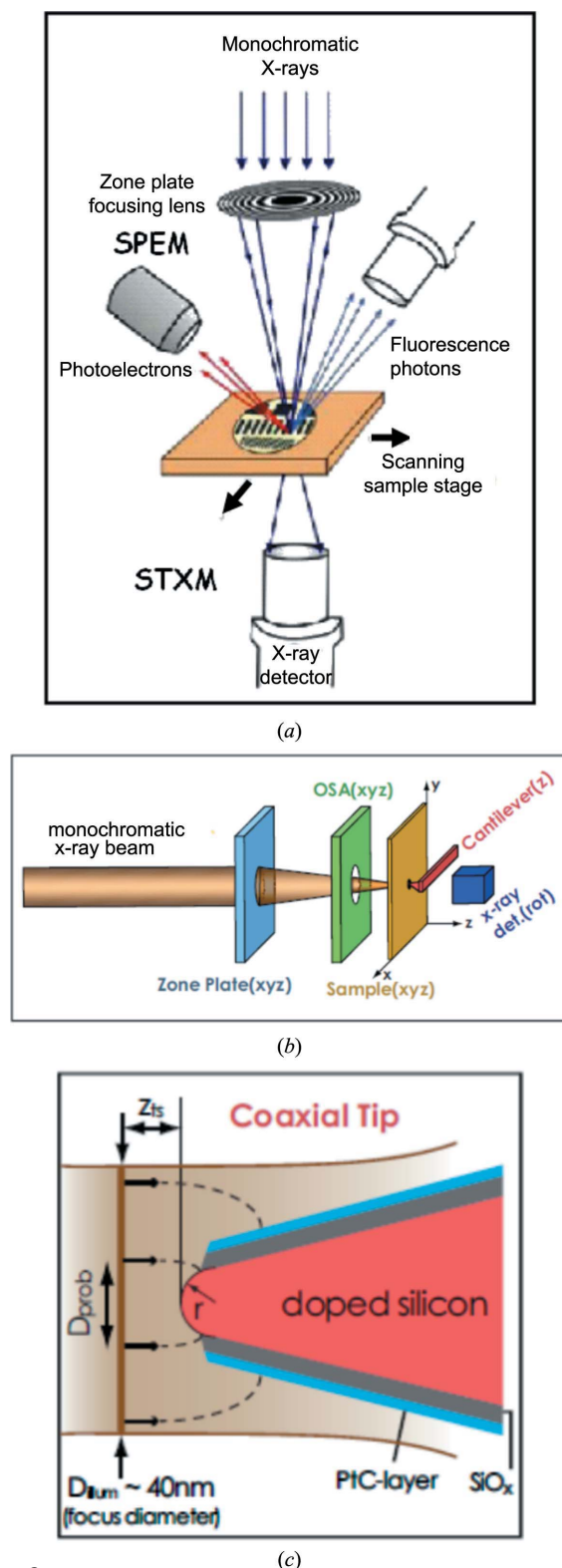
Figure 2
Instrumentation for X-ray imaging. (*a*) Schematic of ZP-focused microscopes for scanning transmission X-ray microscopy (STXM) and scanning photoelectron microscopy (SPEM). (*b*) Set up for nano-X-ray absorption at the Swiss Light Source (Schmid *et al.*, 2010) using a scanning probe tip to localize signal below the X-ray spot size. (*c*) Details of the interaction region of the tip, sample and X-rays (Schmid *et al.*, 2010). [Sources: (*a*) adapted from J. Stöhr, used with permission; (*b*, *c*) from Schmid *et al.* (2010), used with permission from *Ultramicroscopy via* RightsLink license 3398911389610.]

than the far-field diffraction limit to resolution (see Fig. 1). An emerging and very promising technique to achieve even higher spatial resolution is to operate a scanning probe microscope, typically a scanning tunneling microscope (STM), with the sample–tip junction illuminated by ZP-focused soft X-rays. Modulation of the X-ray intensity induces a modulation of the STM signal to the extent that X-ray photo-ionization contributes to that detected signal. Encouraging preliminary results have been obtained (Eguchi *et al.*, 2006) and the nano-XAS at the Swiss Light Source (SLS) beamline is dedicated to development and exploitation of STM–STXM (Schmid *et al.*, 2010). Fig. 2(*b*) is a sketch of the SLS nano-XAS instrument while Fig. 2(*c*) presents details of the tip–sample–X-ray interaction region. Instrumentation for STXM at 2–4 keV (tender X-ray) (Salome *et al.*, 2000; Thieme *et al.*, 2010; Andrade *et al.*, 2011) and at $E > 4$ keV (hard X-ray) (Chen *et al.*, 2014) is conceptually similar, although the details differ since (i) the focal length is much longer at shorter wavelengths providing more space and relaxing the precision required, at least in the X-ray propagation direction, (ii) ZPs must be much thicker and are fabricated using different technologies, (iii) phase contrast and X-ray fluorescence yield techniques are much more effective than transmission, photoelectron or Auger electron detection due to the low-absorption cross sections and low photoelectron yields at higher photon energy.

Coherent diffractive imaging (CDI), in particular Bragg- and ptychography-based approaches, are a set of emerging microscopy techniques that push X-ray imaging resolution towards sub-nanometer, beyond the limitations of state-of-the-art X-ray focusing optics. The capabilities of these techniques enable a number of unresolved questions connecting structure and function of energy materials to be addressed. These CDI techniques are described in detail in another paper in this issue (Thibault *et al.*, 2014) and we only briefly explain them here. Fig. 3 shows typical instrumentation for CDI. In Bragg CDI (Chapman & Nugent, 2010), coherent diffraction patterns are collected from a single particle (or grain) near a Bragg (diffraction) peak at different rotation angles of the particle (Fig. 3*a*) and the contrast mechanisms include three-dimensional strain. Ptychography (Fig. 3*b*) combines point probe scanning with detection of the coherently scattered X-rays after the sample. Overlapping spots on a sample are illuminated with a coherent X-ray beam and extended structures can be imaged with contrast mechanisms sensitive to element, chemical and magnetic content. Combining both techniques, Bragg ptychography (Robinson & Harder, 2009; Godard *et al.*, 2011) can be used to image strain in 3D on extended structures such as nanowires and thin films (Fig. 3*c*). In these techniques, complicated reconstruction algorithms are used to reconstruct the images (see Thibault *et al.*, 2014), but these are beyond the scope of this article.

Fig. 4 provides a recent example in which STXM on beamline 11.0.2 at the Advanced Light Source (ALS) was used to compare normal STXM and soft X-ray ptychography. Figs. 4(*a*) and 4(*b*) are STXM optical density (OD) images at 710 eV (peak Fe L_3 absorption of magnetite) of several
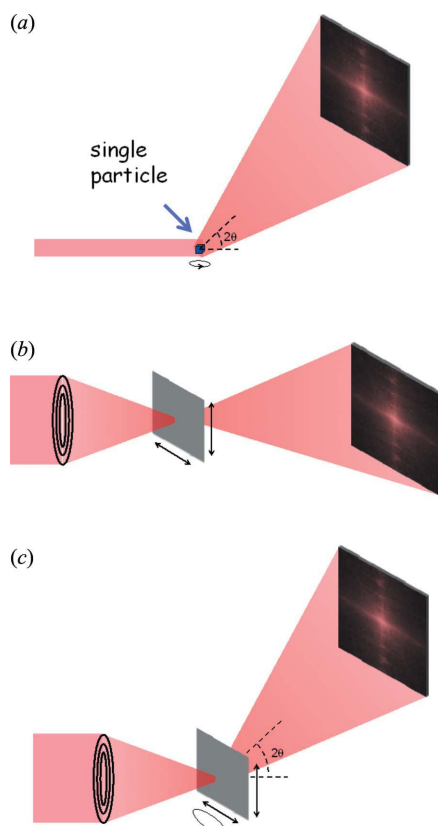
Figure 3
Schematic of (a) Bragg coherent diffraction imaging (CDI), which is sensitive to strain, (b) ptychography, or scanning CDI, and (c) Bragg ptychography, which combines the strain sensitivity of Bragg CDI and the benefit of ptychography to image extended structures.

Figure 4
(a) STXM OD image of two *Magnetospirillum magneticum* strain AMB-1 magnetotactic bacterial cells measured at 710 eV, peak of Fe L_3 absorption. The dotted lines outline the individual cells. (b) STXM OD image of the magnetosomes in the AMB-1 cells [region outlined in (a)] measured at 710 eV with a ZP with a 25 nm outer zone width [diffraction-limited spatial resolution (Raleigh criterion) is 31 nm] (10 nm pixels, 4 ms pixel^{-1}). (c) Image of the same region derived from a ptychography measurement at 710 eV, recorded using the same STXM instrument but with a ZP with a 60 nm outer zone width. The estimated spatial resolution of the ptychographic result is 10 nm. (d)–(f) Ptychography images of a magnetosome chain recorded at 708.2 eV with (d) left and (e) right circular polarized light, and (f) their difference (XMCD). Measurements performed at STXM 11.0.2 at the Advanced Light Source.

Magnetospirillum magneticum strain AMB-1 magnetotactic bacterial cells, and their magnetosomes. Fig. 4(c) shows the same region as for Fig. 4(b), measured using ptychography at 710 eV. The improved spatial resolution is clearly indicated by the much sharper boundaries of the individual magnetosomes and the detection of a third small magnetosome in the lower chain. This study demonstrates the enhanced spatial resolution (relative to conventional STXM) which can be achieved with the addition of a suitable detector to measure the post-specimen coherent scattering signal. A three- to four-fold improvement in spatial resolution was achieved. The ptychography measurement used a low-resolution ZP (60 nm outer zone width) and a direct X-ray sensitive camera which had a very slow readout, which limited the duty cycle (fraction of time measuring) to about 10%. With a more efficient and sensitive camera, it is expected that acquisition times for a ptychography image will be comparable with that for a conventional bright-field STXM image with a point spacing at the effective ptychographic resolution. The ptychography signal is a combination of the real (scattering) and imaginary (absorption) response of the sample to the X-ray beam. Since these signals have different spectral properties, there is every reason to believe there will be new physics and analytical value to spectro-ptychography. There are very few reports of the spectral variation of ptychography, one of them being an O
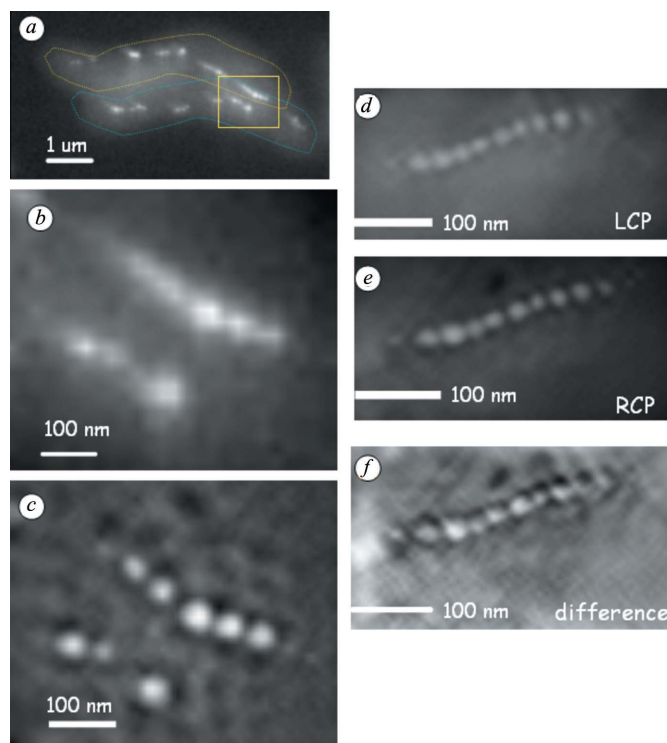
1s study of a mixture of SiO_2 and polymethyl-methacrylate microspheres by Beckers *et al.* (2011). In that work the phase signal derived from the ptychography was found to have a very different spectral response from the absorption signal. Figs. 4(d)–4(f) demonstrate that the ptychography signal is sensitive to magnetism through X-ray magnetic circular dichroism (XMCD) at 708.2 eV, the energy of the maximum intensity of XMCD of magnetite. Unfortunately it was not possible to explore deviations from absorption-based XMCD by performing a full spectro-ptychography investigation due to insufficient measurement time.

3. Predicted improvements with DLSR

What are the gains one can expect for migrating these coherence-limited microscopies from third-generation facilities to a DLSR? Since ZPs can be considered a coherent filter, the efficiency of a given ZP should be improved and there should be some gain in spatial resolution. However, this is not guaranteed; there have even been suggestions that some ZPs

perform better with partially coherent light (Thieme, 1988). Practical experience has been that, while overly large coherence-generating pin holes do lead to detectible degradation of the spatial resolution, the improvements in spatial resolution stop well before the theoretical pin hole size needed to achieve full coherence is reached (Jacobsen *et al.*, 1991). Perhaps this is due to ZP imperfections limiting performance. Measurements of the point spread function over a number of different STXMs and ZPs has shown that even ZPs considered to be state-of-the-art have significant aberrations (Leontowich *et al.*, 2011). If it is ZP quality rather than coherence that limits the performance of present-day STXMs, then significant improvements in ZP technologies will be required in order to fully achieve the promise of DLSRs.

For CDI and ptychography-based approaches using a DLSR, the principle gain is the greatly improved resolution due to the dramatically increased coherent flux, especially in the hard X-ray regime. The improvements are dramatic enough that atomic resolution (0.2 nm) should be possible, at least for materials that are radiation resistant and with high-atomic-number elements. For example, calculations have shown that, for radiation-tolerant high-Z (*e.g.* Au) nanoparticles, true atomic resolution (0.2 nm) is achievable (Huang *et al.*, 2012). For NSLS-II, it is predicted that 1 nm resolution is possible with only a few seconds of data accumulation (Shen *et al.*, 2004). Expected improvements in focusing optics, which should provide better and more stable wavefronts, may also improve (or make easier) ptychography. However, in order for these gains to be realised, beamline stability must also be significantly improved.

There will be a number of other challenges that must be overcome to fulfil the DLSR promise in the area of reciprocal- and real-space spectromicroscopy. Assuming the major goal is better performance in terms of spatial resolution, this will mean using a larger dose density. Many STXM experiments are already using the minimum possible dose to avoid artifacts from radiation damage (*i.e.* many existing STXM studies on soft matter and biological samples are limited by radiation damage rather than microscope performance or available beam time) (Howells *et al.*, 2009). Strategies to reduce damage rates must be developed and used on a routine basis. Measuring samples at low temperature (100 K or lower) is known to preserve morphology, limit mass loss effects and stop radiolysis processes in hydrated samples (Echlin, 1992). However, it has been shown that, at least for polymer materials, the rate of spectral changes (bond breaking) is not affected by cooling (Beetz & Jacobsen, 2003). For wet samples, where radiation-generated radials and ions can lead to chain reaction damage mechanisms, freezing the water to reduce radical and ion mobility is an effective damage-reduction method (Chen *et al.*, 2014; Echlin, 1992). Freeze-drying biological samples is also a promising method in some systems (Zierod, 1988). Another possible concern with the increased brightness of DLSRs is sample heating. While this will be a very serious problem with techniques using the full power of an insertion device (as it already is for most third-generation ID beamlines), beam heating is probably of little concern for ZP focusing optics which focus as little as a few percent of the light impinging on the ZP into the spot used for imaging. Although ptychography is typically measured using higher flux, that flux is spread over a larger area, such that the local heating is not expected to be a serious problem.

As pointed out by Howells *et al.* (2009), the scattering signal in a two-dimensional pixel or three-dimensional voxel scales as the fourth power of the spatial resolution, and thus the practical spatial resolution scales as the inverse fourth power of the absorbed dose. At the same time, the Rose criterion predicts the minimum dose required to achieve a specific spatial resolution for a given system. Howells *et al.* provide a method to understand the limitations that radiation damage will place on ultra-resolution X-ray imaging (see Fig. 3 of their paper). Their plots of the maximum tolerable dose and the minimum dose required for imaging as a function of spatial resolution for proteins, both dry and in aqueous solution, are very instructive when considering radiation dose limitations on X-ray imaging. Their evaluation suggests that achieving a spatial resolution better than 10 nm for proteins in wet biological systems will be very difficult. Radiation damage is predicted to ultimately limit the achievable spatial resolution in many systems, particularly polymeric or biological soft matter, which have much lower critical doses for radiation damage than metal or semiconductor systems. The temporal width of a single pulse in a DLSR is many times longer than the nuclear motion leading to bond breaking, in contrast to the femtosecond pulses of free-electron lasers (FELs). Thus diffract-then-destroy methods emerging in fourth-generation FELs are not likely to be implementable in a DLSR. Cryo-methods for reducing mass loss and restricting radical and ion mobility are likely to be the most effective method of controlling radiation damage. Thus reliable cryo-sample technologies should be actively developed for DLSR imaging facilities.

Higher signal rates are expected for DLSR systems, as compared with existing third-generation facilities. At present, signal rates in undulator-based soft X-ray STXMs at the ALS and Canadian Light Source (CLS) are limited by detector performance rather than source, beamline or ZP performance. The preferred bright-field detector at most existing soft X-ray STXMs uses a fine grain size scintillator to convert soft X-rays to visible light, followed by a high-performance photomultiplier (Kilcoyne *et al.*, 2003, 2010). This system has a maximum linear count rate of 20 MHz whereas the ALS and CLS undulator STXMs can produce 500 MHz in the diffraction-limited ZP-focused spot over wide energy ranges. Avalanche photodiodes operating in single-photon-counting mode are used at count rates up to 100 MHz (Nolle *et al.*, 2012) but they are much less efficient, and do not work effectively below 500 eV. Improved single-photon-counting detectors for conventional STXM and higher sensitivity and higher dynamic range cameras for ptychography are urgently needed if the full potential of X-ray imaging at DSLRs is to be realised. In the latter context, Dectris (http://www.dectris.com) already sells single X-ray sensitive cameras for hard X-rays with high dynamic range and fast readout. Dectris has a

project to extend their technology into the soft X-ray and there is a Department of Energy collaboration (BNL, APL, APS) which has recently developed a new pixel detector for soft X-rays with high dynamic range and ultrafast readout. For soft X-ray ptychography it should also be possible to develop high-efficiency soft X-ray sensitive scintillator screens which would convert X-rays to visible photons which could then be imaged with very high dynamic range, efficiency and fast readout using modern visible-light cameras recently developed for super-resolution laser fluorescence imaging.

4. Examples of present-day applications of real- and reciprocal-space chemical imaging to energy materials

Hydrogen-burning polymer-electrolyte-membrane fuel cells (PEM-FCs) have tremendous promise to reduce and eventually eliminate use of fossil fuels for mobile power applications, and thus this technology (which is already mature and commercially successful for stationary and fleet applications) is planned to be implemented by several major manufacturers in mass-produced personal automobiles in the near future. One of the analytical challenges to further improvements in the materials used for automotive PEM-FCs is visualizing and quantifying the spatial distribution of the ionomer component in PEM-FC cathodes. The ionomer is a perfluorinated sulfonic acid (PFSA) material which provides a pathway for ionic conduction of H$^+$ inside the cathode. The protons are generated at the anode and transported through the PFSA membrane to the cathode under the influence of the field associated with the potential generated by the electrochemical oxidation of H$_2$ to H$_2$O. While transmission electron microscopes equipped with X-ray fluorescence or energy-loss detection have the potential to measure ionomers in PEM-FC cathodes, few successful studies have been reported. Most attempts are unsuccessful due to the very high radiation damage rate which leads to loss of the F atoms of the PFSA ionomer. For several years now, soft X-ray STXM studies at the C 1s and F 1s edges have been used to provide a reliable means to visualize and quantitatively map ionomers in PEM-FC cathodes (Susac $et\ al.$, 2011, 2013; Hitchcock $et\ al.$, 2014; Berejnov $et\ al.$, 2014). Fig. 5 illustrates the principles

and documents a few-energy imaging method which is an efficient way to measure ionomer distributions in PEM-FC devices (Susac $et\ al.$, 2013). The results in Fig. 5 were obtained using images at only four photon energies, in order to examine large areas of each sample, and many samples. More detailed results are obtained if image sequences are recorded with fine energy spacing such that there is a detailed spectrum at each pixel. Analysis of such spectromicroscopy stacks (Jacobsen $et\ al.$, 2000) using quantitative reference spectra (see Fig. 5b) allows quantitative maps for each chemical component in the system (Ade & Hitchcock, 2008; Howells $et\ al.$, 2007; Hitchcock, 2012). Fig. 6 presents component maps for the carbon support, the ionomer and the Pt catalyst, as well as a colour-
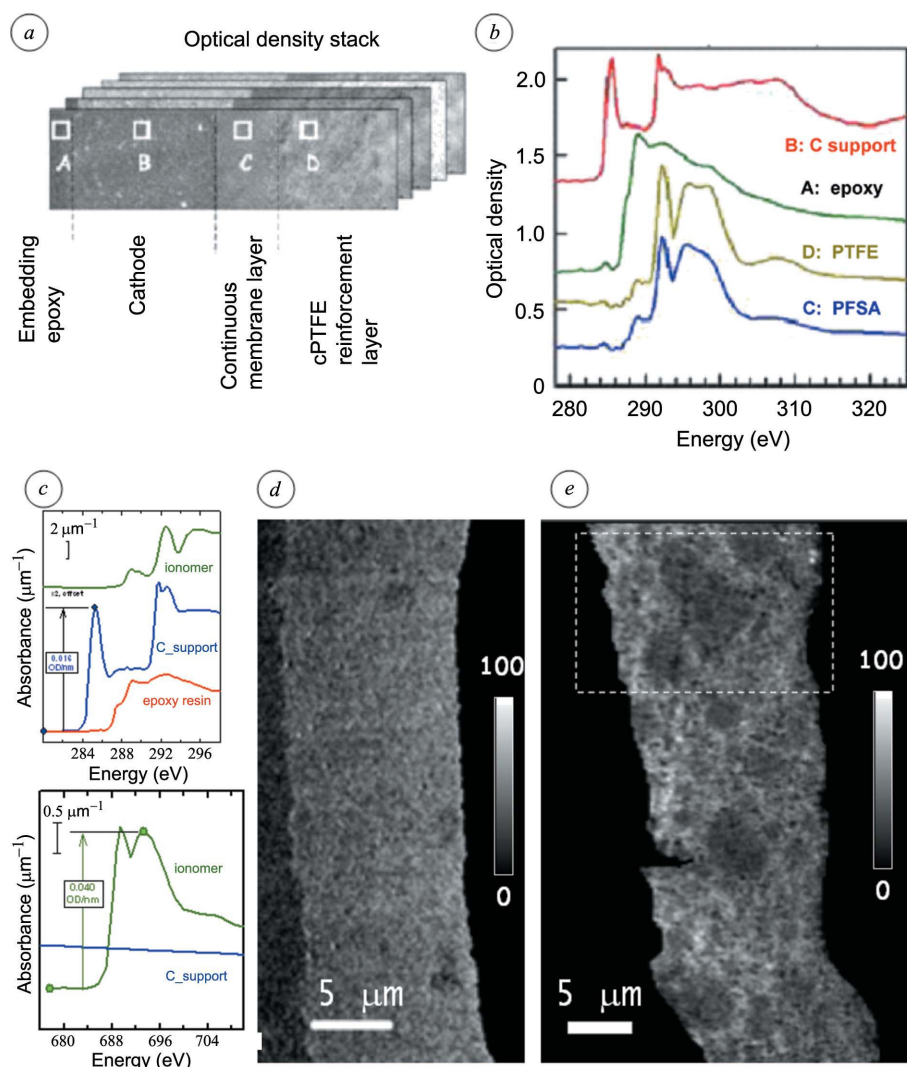

Figure 5
Example of energy materials research with STXM. (a) Principles of ionomer mapping using C 1s and F 1s spectromicroscopy in STXM, used to measure ionomer distributions in the catalyst layer structures of cathodes in PEM-FCs under development for automotive use. (b) C 1s reference spectra of the chemical components. (c) C 1s and F 1s spectra on optical density per nanometre of chemical components, illustrating the principles for quantitative mapping. Ionomer maps in cathodes derived from two energy F 1s STXM stack maps for a (d) catalyst-coated membrane and a (e) catalyst-coated gas diffusion layer (Susac $et\ al.$, 2013). The dashed rectangle in (e) shows the region of the gas diffusion layer selected for a full C 1s stack analysis (see Fig. 6). The perfluoro sulfonic acid (PFSA) membrane signals (located on the right with respect to the cathode layer) have been masked off in (d) and (e).
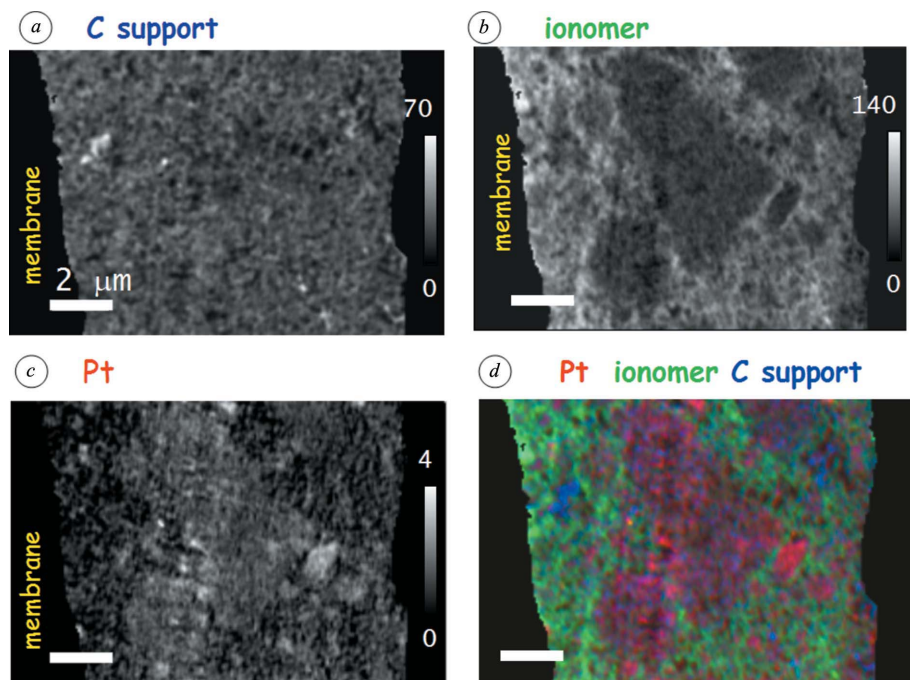
Figure 6
Component maps for (*a*) the carbon support, (*b*) the ionomer and (*c*) Pt, derived from fitting a full C 1*s* stack of a cathode catalyst layer in the gas diffusion layer structure (region selected in Fig. 5*e*). (*d*) Re-scaled colour composite of the Pt (red), ionomer (green) and carbon support (blue) component maps. Scale bars are 2 μm; grey intensity bars represent thickness in nanometres.

and the environment of the sample (humidity, temperature, gas composition, *etc.*) are critical variables. While a lot can be learned from comparisons of post-use and virgin samples, the X-ray spectromicroscopy results would have greater impact if they were measured on samples under realistic conditions (*i.e.* 'in situ'). Even more preferable would be if the studies could be carried out under conditions which would allow the device itself, or an abstracted component of it, to be subjected to spectromicroscopy or coherent diffraction imaging studies while actually operating (so-called *operando* studies). Owing to longer working distances, hard X-ray spectromicroscopy and diffraction methods have a clear advantage for both *in situ* and *operando* studies (Nelson *et al.*, 2012). Still there are already some results from *in situ* soft X-ray STXM studies of PEM-FC (Berejnov *et al.*, 2011) and batteries (Chueh *et al.*, 2013), while *operando* photoemission studies have been performed on PEM-FC (Casalongue *et al.*, 2013) and Li battery samples (Liu *et al.*, 2013). The higher performance expected from DLSR microscopes will enable further advances in *in situ* and *operando* science.

coded composite for a region of the cathode [see Fig. 5(*e*) for location of the analyzed region] derived from a C 1*s* image sequence recorded over a 12 μm × 18 μm area with 160 × 240 pixels at 60 photon energies. Such fine-detailed images provide insights useful to understand degradation processes (by comparing the same material before and after operational testing) and help improve processing methods (*e.g.* by improving mixing in cathode inks to avoid the uneven ionomer distribution clearly observed in this sample).

STXM has been applied to PEM-FC issues in a number of ways other than two-dimensional projection mapping of the chemical components of cathodes. In an ideal structure there would be a conformal coating of ionomer on the Pt-catalyst-coated carbon support particles. That coating would be at an optimal thickness (sub-10 nm) and there would be continuous pathways for proton conduction through the ionomer layer from the membrane to the opposite side of the cathode, and a continuous open path for the product water to be removed. Materials and process optimization to achieve such an ideal structure requires visualization and quantitation of the chemical structure in 3D. Using angle-scan STXM spectro-tomography, measurements of the porosity and ionomer in cathodes in 3D have been made recently (Berejnov *et al.*, 2013). Carrying out such experiments on a higher-performance DLSR STXM would have significant advantages in terms of data quality, speed and spatial resolution.

A very important aspect of energy materials optimization is that the materials are not used under dry isolated conditions, but rather they are part of complex systems where interfaces

5. Some examples of 'impossible' or dream experiments that may be do-able on a DLSR

5.1. Artificial photosynthesis and organic photovoltaics

X-ray analyses are the premier tool for atomic-scale structural studies. X-rays are being used to study amorphous metal-oxide water-splitting catalyst films that are an emerging class of solar fuels catalysts electrolytically deposited from simple inorganic solution state precursors (Kanan & Nocera, 2008; Chen *et al.*, 2010). Synchrotron X-ray spectroscopy (Blakemore, 2013) and scattering (Du, 2012) studies have revealed that the amorphous oxides are composed of molecular-dimensioned ligand-capped metal-oxo domains that mimic the Mn_4CaO_4 cluster catalyst central to biological photosynthesis. Progress in biomimetic artificial leaf devices requires *in operando* characterization of light-harvesting and catalytic layers, that is both spatially and temporally resolved. The DLSR capability to deliver intense, collimated, nanoscale-focused, soft and hard X-ray beams offers unprecedented opportunities to achieve dynamically resolved structure profiling of light-harvesting and catalytic active layers under functional conditions. These new capabilities include nano resonant inelastic X-ray scattering, nano X-ray absorption, nano ambient pressure X-ray photoelectron spectroscopy,
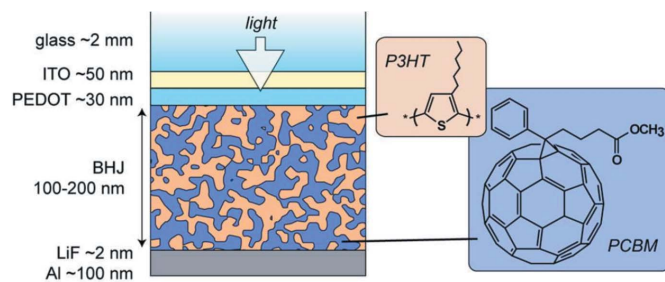
Figure 7
Cartoon of the idealized structure of bulk hetero-junction (BHJ) photovoltaic devices based on PCBM (electron acceptor) and P3HT (electron donor). To date, neither real-spacing or reciprocal-space analysis have identified an actual structure that achieves complete phase separation.

ptychography and X-ray photon correlation spectroscopy to map chemical and atomic structure and kinetics.

Organic photovoltaics (OPVs) are of increasing interest as a potential source of renewable and economically viable electric energy (Collins *et al.*, 2013). Recently, the power conversion efficiency for organic solar cells based on solution-processable blends of conjugated polymers and fullerenes has surpassed 8% with the materials PTB7 (poly{4,8-bis[(2-ethylhexyl)oxy]-benzo[1,2-*b*:4,5-*b'*]dithiophene-2,6-diyl}{3-fluoro-2-[(2-ethylhexyl)carbonyl]thieno[3,4-*b*]thiophenediyl}) and [6,6]-phenyl-C_{71}-butyric acid methyl ester ($PC_{71}BM$). This has been achieved through a combination of materials optimization (for example, use of C_{70} rather than C_{60} fullerene) as well as process optimization resulting in improved interfaces within the materials and with device electrodes (He *et al.*, 2011). The nanoscale and mesoscale morphologies of these blends are critical for device performance. The currently accepted model is that of a bulk heterojunction (BHJ) blend (see Fig. 7) in which absorption of visible light creates electron–hole pairs that diffuse to the interface of electron donor and acceptor materials. The subsequent separation of the electron and hole along with a continuous path for each charge carrier to the appropriate electrode is facilitated by small domain sizes and a bicontinuous nature of the material's morphology. Owing to

the short lifetime and limited exciton diffusion length, a domain size of $\sim$10 nm is thought to be ideal since this is close to the diffusion length of the excitons created upon photo-absorption. Polymer crystallinity may be beneficial to device performance in some systems as absorption and charge transport are both enhanced. However, some of the best performing materials (*e.g.* PTB7:$PC_{71}BM$ based devices) have negligible crystallinity and the non-crystalline regions are not pure but rather contain a mixture of the fullerene acceptor and donor polymer. In the polymer-fullerene family of OPVs the impact of the miscibility of donor and acceptor is not well understood, largely because it is difficult to quantitatively measure the spatial distributions of the organic components in actual devices. Better understanding of such materials has been obtained by a combination of soft X-ray scattering (both resonant and non-resonant) and chemically specific real-space imaging using STXM (Collins *et al.*, 2013). Fig. 8 shows a cartoon of the structures of blends of PTB7 and $PC_{71}BM$ without (Fig. 8*a*) and with (Fig. 8*b*) a di-iodo-octane (DIO) additive, based on this research (Collins *et al.*, 2013). The DIO additive greatly reduces domain size, and increases the fraction of the material at the interface of the acceptor and donor domains. Fig. 8(*c*) shows a cartoon of the exciton generation process at the interface illustrating the efficient charge separation at the nano-scale interfaces and minimal loss of efficiency through electron–hole recombination in larger domains. While this model is very seductive, it is only partially based on actual measurements due to the limitations of the current generation of X-ray sources, microscopes and scattering instrumentation. In particular, although the theoretical diffraction-limited resolution of the STXM used for these studies is 31 nm, quantitative measurements become unreliable for features at a far larger scale (perhaps 50–70 nm) due to wings in the point spread function of the instrument such that the spectral signal has contributions at much larger scales than the nominal ZP focal point size. This adds in signals from adjacent domains, artificially reducing the measured domain purity (Collins & Ade, 2012). The much larger coherence of a DLSR source, combined with improved ZPs and scanning mechanisms, will result in much more reliable quantitative
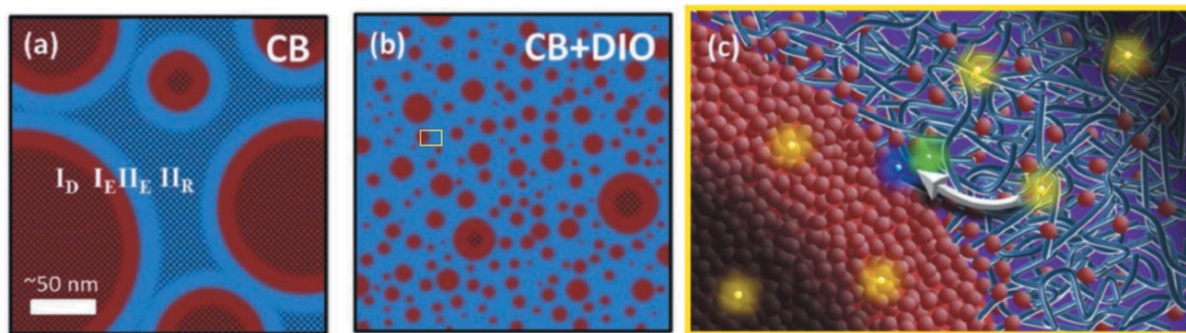

Figure 8
Cartoon of the structure of the PTB7:$PC_{71}BM$ organic photovoltaic material without (*a*) and with (*b*) di-iodo-octane (DIO) additive. These cartoons illustrate conclusions derived from soft X-ray spectromicroscopy and resonant scattering studies (Collins *et al.*, 2013). (*c*) Cartoon of the exciton generation process at the interface of the two types of domains. [Adapted from Collins *et al.* (2013), J. Wiley & Sons, used with permission from *Advanced Energy Materials via* RightsLink license 3399391012977.]

compositional analysis at the sub-20 nm scale, which will have a tremendous impact on the understanding of BHJ-based organic photovoltaics, which may lead to improved devices. Polarization-dependent absorption and resonant soft X-ray scattering studies are also important as these have already given useful insights into non-crystalline orientational ordering in organic photovoltaic films (Collins *et al.*, 2012).

While high-spatial-resolution quantitative imaging of energy materials in two (Collins *et al.*, 2013) and three dimensions (Berejnov *et al.*, 2013) will significantly improve with DLSRs, another very important area where game-changing improvements are to be expected is *in situ* and *operando* studies of energy materials. Recent research of this type includes: in photovoltaics, biased (Lafford *et al.*, 2013) and electron-beam-induced current studies (Watts *et al.*, 2009); in battery materials, model systems (Nelson *et al.*, 2012; Chen *et al.*, 2010); in PEM-FCs, full-fledged *operando* systems (Casalongue *et al.*, 2013). Such studies will be greatly enhanced by the larger coherence and improved source stability in DLSRs.

5.2. Three-dimensional imaging with nano-tomography

Owing to low absorption contrast, it is essential to use tomographic methods to achieve the full potential of nano-focused probes at high photon energies (Withers, 2007). Existing hard X-ray tomography systems using focused probes typically achieve a spatial resolution of a few hundred nanometres, although recently a point focus of less than 5 nm at 8 keV has been achieved using a combination of a pre-focus Kirkpatrick–Baez mirror and a W/Si multilayer ZP (MZP) (Döring *et al.*, 2013). However, the working distance of that system is only 50 μm and the depth of focus is of the order of a micrometre, which would make tomographic measurements very challenging. When combined with a high-performance X-ray detector it is possible to use hard X-ray nanoprobes to make three-dimensional elemental maps, such as that of various metal species in the diatom species, *Cyclotella mene-ghiniana* at 400 nm spatial resolution (Fig. 9), reported by de Jonge *et al.* (2010). Further details of the present capabilities and future potential of hard X-ray nano-tomography with X-ray fluorescence detection are provided in this issue (de Jonge *et al.*, 2014). The higher brightness and coherence of DLSRs will improve the optical efficiency significantly, and that, combined with improved energy-dispersive array detectors, should enable this type of fluorescence mapping (de Jonge *et al.*, 2010) and fluorescence-yield hard and soft X-ray absorption studies (Hitchcock *et al.*, 2012) to be performed at sub-10 nm spatial resolution. The HXN beamline at NSLS-II has a target of performing tomography at 1 nm
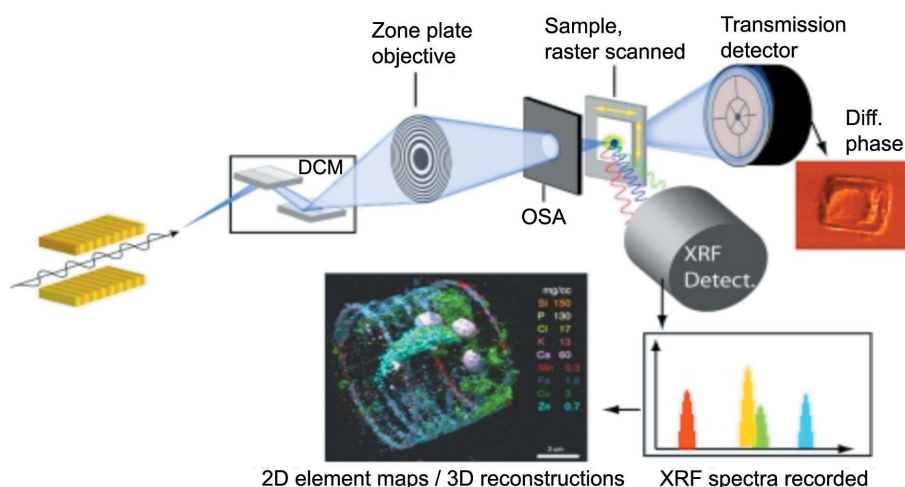

Figure 9
Schematic and colour-coded multi-element three-dimensional visualization of *Cyclotella mene-ghiniana* (a diatom) from an X-ray fluorescence tomography measurement [reproduced from de Jonge *et al.* (2010), copyright, Martin de Jonge].

spatial resolution. Using hard X-ray ptycho-tomography at PETRA-III (Thibault *et al.*, 2014), a three-dimensional voxel resolution of 10 nm in all three dimensions has been achieved (Schropp *et al.*, 2012; Stephan, 2013).

5.3. X-ray imaging at sub-1 nm spatial scale

We now return to the analytical challenge of visualizing the spatial morphology within the PFSA membranes that provide proton conduction inside PEM-FCs. Soft X-ray ptychography in transmission [or forward (*e.g.* small-angle) scattering] mode (Thibault *et al.*, 2014) offers the possibility of reconstructing sub-nanometre molecular arrangements. There is also the possibility of such measurements *in situ* in humid environments (which is the case for operating PEM-FCs), and this has been achieved (at much lower spatial resolution) in both soft X-ray (Berejnov *et al.*, 2011) and hard X-ray studies (Dixon *et al.*, 2012). By making use of the strong chemical sensitivity of absorption (Susac *et al.*, 2011, 2013; Hitchcock *et al.*, 2014; Berejnov *et al.*, 2014; Collins & Ade, 2012) and resonant soft X-ray scattering (Collins *et al.*, 2012, 2013) at the S 2*p*, C 1*s*, F 1*s* and S 1*s* edges one can measure the distribution of molecular species in these membranes. This direct molecular information would profoundly improve our understanding of these complicated nanostructures. A similar approach could be applied to OPV blends. The ultimate limiting factor here will be radiation damage to the membranes. Based on quantitative studies using soft X-ray STXM, the critical dose for dry membranes is of the order of 50 MGy. The critical dose is much lower for wet membranes at room temperature due to radiolysis (Hitchcock, unpublished results).

5.4. *Operando* imaging of individual catalyst and energy storage particles

One of the holy grails for energy nanosciences is the observation of the atomic structure of individual nanoparticles in 3D while they are functioning. This goal is important to

existing and emerging energy technologies, including catalysis, artificial photosynthesis, fuel cells, batteries and smart windows. The improved performance of DLSRs offers the potential to move towards this goal by providing sufficient coherent flux for atomic-scale studies of nanoparticle structure. Understanding the 3D structure and how this evolves during operation of the battery will provide new insights. A DLSR will provide the coherent flux necessary for spectroscopic imaging of nanoparticles at the nanometre scale. Understanding the 3D structure through ptychographic imaging and the local chemistry and charge transfer through nano-X-ray absorption spectroscopy and nano-X-ray emission spectroscopy will allow dramatic advances in understanding this important class of materials. Radiation damage will ultimately limit the chemical sensitivity achievable at high spatial resolution, as outlined earlier.

Battery electrode materials often employ nanoparticles ($\sim$100 nm diameter) to increase the charge/discharge rates and to mitigate the negative impact of these typically high-resistivity materials. The behaviour of these particles during battery cycling is complicated and poorly understood. In Li-ion batteries we do not know how the individual particles undergo phase transformations, how Li diffuses into and through the lattice, and how the solid electrolyte interface influences charge/discharge (Fig. 10). These processes depend on the properties of the individual electrode nanoparticles, but since most experiments probe ensembles of particles or are not conducted *in operando* we do not understand this relationship in any detail. Atomic-resolution CDI techniques enabled by the DLSR will lead to groundbreaking experiments observing the atomic structure of individual nanoparticles *in operando*. Nanoprobe hard and soft spectroscopies will allow measurement of local electronic and chemical structure at nanometre spatial resolution to study the above issues.

Similarly, nanoparticles (<10 nm) control heterogeneous catalytic activity, although the precise relationship between nanoparticle surface structure and reactivity is poorly under-

stood. For example, nanoparticles with different sizes have different lattice terminations and surface defects that can provide sites with unique catalytic properties. If we knew what particle properties resulted in these reactive sites, we could synthesize ensembles of catalyst particles that all have extremely high selectivity and activity, enabling revolutionary heterogeneous catalysis. While much work has been done on supported nanoparticle catalysts using X-ray spectromicroscopy methods (Smit *et al.*, 2009; Cats *et al.*, 2013) and analytical electron microscopies, *in operando* studies at the single nanoparticle level would be groundbreaking.

6. Summary

Here we have described current and future capabilities of X-ray spectromicroscopy and coherent imaging methods that will benefit from the huge brightness increase that will be available at DLSRs. The emphasis has been on energy materials applications and the new science of these enabled by DLSRs. Most exciting are the potential 'dream experiments' that are presently impossible with current capabilities. We have described several of these, including the prospect of imaging the spatial morphology in perfluorinated sulfonic acid membranes and ionomer distributions in cathodes of polymer electrolyte membrane fuel cells, mesoscale domain formation in organic photovoltaics, and observation of the atomic structure of individual catalyst particles while they are functioning (*operando*).

Figure 10
Schematic of battery electrode particle illustrating pathways for lithiation through the solid–electrolyte interface (SEI) layer (blue) to react and form a Li-rich phase (red). The SEI forms at the electrode from reaction of the electrolyte with the electrode and Li species.

References

Ade, H. & Hitchcock, A. P. (2008). *Polymer*, **49**, 643–675.
Andrade, V. D., Susini, J., Salome, M., Beraldin, O., Rigault, C., Heymes, T., Lewin, E. & Vidal, O. (2011). *Anal. Chem.* **83**, 4220–4227.
Beckers, M., Senkbeil, T, Gorniak, T., Reese, M., Giewekemeyer, K., Gleber, S.-C., Salditt, T. & Rosenhahn, A. (2011). *Phys. Rev. Lett.* **107**, 208101.
Beetz, T. & Jacobsen, C. (2003). *J. Synchrotron Rad.* **10**, 280–283.
Berejnov, V., Susac, D., Stumper, J. & Hitchcock, A. P. (2011). *ECS Trans.* **41**, 395–402.
Berejnov, V., Susac, D., Stumper, J. & Hitchcock, A. P. (2013). *ECS Trans.* **50**, 361–368.
Berejnov, V., Susac, D., Stumper, J., Lee, V. & Hitchcock, A. P. (2014). *Energy Environ. Sci.* In preparation.
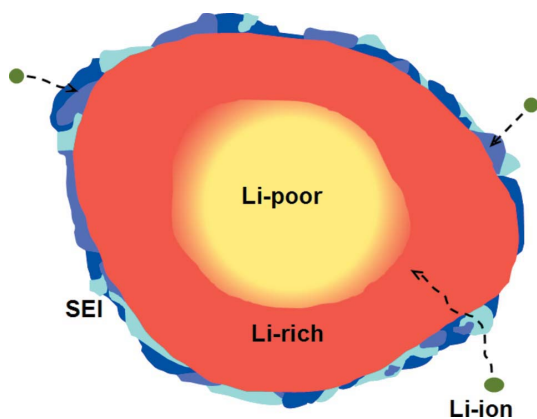Blakemore, J. D. (2013). *Inorg. Chem.* **52**, 1860–1871.

Casalongue, H. S., Karp, S., Viswanathan, V., Miller, D. J., Friebel, D., Hansen, H. A., Nørskov, J. K., Nilsson, A. & Ogasawara, H. (2013). *Nat. Commun.* **4**, 2817.

Cats, K. H., Gonzalez-Jimenez, I. D., Liu, Y., Nelson, J., van Campen, D., Meirer, F., van der Eerden, A. M. J., de Groot, F. M. F., Andrews, J. C. & Weckhuysen, B. M. (2013). *Chem. Commun.* **49**, 4622–4624.

Chao, W., Fischer, P., Tyliszczak, T., Rekawa, S., Anderson, E. & Naulleau, P. (2012). *Opt. Express*, **20**, 9777–9783.

Chapman, H. N. & Nugent, K. A. (2010). *Nat. Photon.* **4**, 833–839.

Chen, S., Deng, J., Yuan, Y., Flachenecker, C., Mak, R., Hornberger, B., Jin, Q., Shu, D., Lai, B., Maser, J., Roehrig, C., Paunesku, T., Gleber, S. C., Vine, D. J., Finney, L., VonOsinski, J., Bolbat, M., Spink, I., Chen, Z., Steele, J., Trapp, D., Irwin, J., Feser, M., Snyder, E., Brister, K., Jacobsen, C., Woloschak, G. & Vogt, S. (2014). *J. Synchrotron Rad.* **21**, 66–75.

Chen, Y., Kanan, M. W., Gorin, C. F., Beh, E. S., Kanan, M. W. M., Yachandra, V. K. & Nocera, D. G. (2010). *J. Am. Chem. Soc.* **132**, 13692–13701.

Chueh, W. C., El Gabaly, F., Sugar, J. D., Bartelt, N. C., McDaniel, A. H., Fenton, K. R., Zavadil, K. R., Tyliszczak, T., Lai, W. & McCarty, K. F. (2013). *Nano Lett.* **13**, 866–872.

Collins, B. A. & Ade, H. (2012). *J. Electron. Spectrosc. Relat. Phenom.* **185**, 119–128.

Collins, B. A., Cochran, J. E., Yan, H., Gann, E., Hub, C., Fink, R., Wang, C., Schuettfort, T., McNeill, C. R., Chabiny, M. L. & Ade, H. (2012). *Nat. Mater.* **11**, 536–543.

Collins, B. A., Li, Z., Tumbleston, J. R., Gann, E., McNeill, C. R. & Ade, H. (2013). *Adv. Energy Mater.* **3**, 65–74.

Debe, M. K. (2012). *Nature (London)*, **486**, 43–51.

Dixon, D., Habereder, A., Farmand, M., Kaserer, S., Roth, C. & Ramaker, D. E. (2012). *J. Phys. Chem. C*, **116**, 7587–7595.

Döring, F., Robisch, A. L., Eberl, C., Osterhoff, M., Ruhlandt, A., Liese, T., Schlenkrich, F., Hoffmann, S., Bartels, M., Salditt, T. & Krebs, H. U. (2013). *Opt. Express*, **21**, 19311.

Du, D. (2012). *J. Am. Chem. Soc.* **134**, 11096−11099.

Echlin, P. (1992). *Low Temperature Microscopy and Analysis*, p. 30. New York: Plenum.

Eguchi, T., Okuda, T., Matsushima, T., Kataoka, A., Harasawa, A., Akiyama, K., Kinoshita, T., Hasegawa, Y., Kawamori, M., Harujama, Y. & Matsui, S. (2006). *Appl. Phys. Lett.* **89**, 2431191.

Falcone, R., Jacobsen, C. J., Kirz, J., Marchesini, S., Shapiro, D. & Spence, J. (2011). *Contemp. Phys.* **52**, 293–318.

Fink, J., Schierle, E., Weschke, E. & Geck, J. (2013). *Rep. Prog. Phys.* **76**, 056502.

Frenkel, A. I. & van Bokhoven, J. A. (2014). *J. Synchrotron Rad.* **21**, 1084–1089.

Godard, P., Carbone, G., Allain, M., Mastropietro, F., Chen, G., Capello, L., Diaz, A., Metzger, T. H., Stangl, T. & Chamard, V. (2011). *Nat Commun.* **2**, 568.

Guenther, S., Kaulich, B., Gregoratti, L. & Kiskinova, M. (2002). *Prog. Surf. Sci.* **70**, 187–260.

He, Z., Zhong, C., Huang, X., Wong, W.-Y., Wu, H., Chen, L., Su, S. & Cao, Y. (2011). *Adv. Mater.* **23**, 4636–4643.

Hitchcock, A. P. (2012). *Soft X-ray Imaging and Spectromicroscopy*, ch. 22, in *Handbook on Nanoscopy*, Vol. II, edited by G. Van Tendeloo, D. Van Dyck and S. J. Pennycook, pp. 745–791. New York: Wiley.

Hitchcock, A. P., Berejnov, V., Lee, V., West, M., Dutta, M., Colbow, V. & Wessel, S. (2014). *J. Power Sources*, **266**, 66–78.

Hitchcock, A. P., Obst, M., Wang, J., Lu, Y. S. & Tyliszczak, T. (2012). *Environ. Sci. Technol.* **46**, 2821–2829.

Howells, M., Jacobsen, C. & Warwick, T. (2007). *Principles and Applications of Zone Plate X-ray Microscopes*, in *Science of Microscopy*, edited by P. W. Hawkes and J. C. H. Spence. New York: Springer.

Howells, M. R., Beetz, T., Chapman, H. N., Cui, C., Holtona, J. M., Jacobsen, C. J., Kirz, J., Lima, E., Marchesini, S., Miao, H., Sayre, D., Shapiro, D. A., Spence, J. C. H. & Starodub, D. (2009). *J. Electron Spectrosc. Relat. Phenom.* **170**, 4–12.

Huang, X., Harder, R., Leake, S., Clark, J. & Robinson, I. (2012). *J. Appl. Cryst.* **45**, 778–784.

Huang, X., Yan, H., Nazaretski, E., Conley, R., Bouet, N., Zhou, J., Lauer, K., Li, L., Eom, D., Legnini, D., Harder, R., Robinson, I. K. & Chu, Y. S. (2014). *Nat. Sci. Rep.* **3**, 3562.

Jacobsen, C., Williams, S., Anderson, E., Browne, M. T., Buckley, C. J., Kern, D., Kirz, J., Rivers, M. & Zhang, X. (1991). *Opt. Commun.* **86**, 351–364.

Jacobsen, C., Wirick, S., Flynn, G. & Zimba, C. (2000). *J. Microsc.* **197**, 173–179.

Jonge, M. D. de, Holzner, C., Baines, S. B., Twining, B. S., Ignatyev, K., Diaz, J., Howard, J. L., Legnini, D., Miceli, A., McNulty, I., Jacobsen, C. J. & Vogt, S. (2010). *Proc. Nat. Acad. Sci.* **107**, 15676–15680.

Jonge, M. de, Ryan, C. & Jacobsen, C. (2014). *J. Synchrotron Rad.* **21**, 1031–1047.

Kanan, M. W. & Nocera, D. G. (2008). *Science*, **321**, 1072–1075.

Kang, H. C., Maser, J., Stephenson, G. B., Liu, C., Conley, R., Macrander, A. T. & Vogt, S. (2006). *Phys. Rev. Lett.* **96**, 127401.

Kilcoyne, A. L. D., Ade, H., Attwood, D., Hitchcock, A. P., McKean, P., Mitchell, G. E., Monteiro, P., Tyliszczak, T. & Warwick, T. (2010). *AIP Conf. Proc.* **1234**, 459–462.

Kilcoyne, A. L. D., Tyliszczak, T., Steele, W. F., Fakra, S., Hitchcock, P., Franck, K., Anderson, E., Harteneck, B., Rightor, E. G., Mitchell, G. E., Hitchcock, A. P., Yang, L., Warwick, T. & Ade, H. (2003). *J. Synchrotron Rad.* **10**, 125–136.

Lafford, T. A., Villanova, J., Plassat, N., Dubois, S. & Camel, D. (2013). *J. Phys. Conf. Ser.* **425**, 192019.

Leontowich, A. F. G., Tyliszczak, T. & Hitchcock, A. P. (2011). *Proc. SPIE*, **8077**, 80770N.

Li, Y., Yasa, M., Pelletier, O., Safinya, C. R., Caine, E., Hu, E. E. & Fernandez, P. (2003). *Appl. Phys. Lett.* **82**, 2538–2540.

Liu, X., Wang, D., Liu, G., Srinivasan, V., Liu, Z., Hussain, Z. & Yang, W. (2013). *Nat. Commun.* **42**, 2568.

Maiyalagan, T. & Pasupathi, S. (2010). *Mater. Sci. Forum*, **657**, 143–189.

Muradov, N. Z. & Veziroğlu, T. N. (2012). Editors. *Carbon-Neutral Fuels and Energy Carriers*, pp. 1–114. Boca Raton: CRC Press.

Nelson, J., Misra, S., Yuan, Y., Jackson, A., Liu, Y., Wang, H., Dai, H., Andrews, J. C., Cui, Y. & Toney, M. F. (2012). *J. Am. Chem. Soc.* **134**, 6337–6343.

Nolle, D., Weigand, M., Audehm, P., Goering, E., Wiesemann, U., Wolter, C., Nolle, E. & Schütz, G. (2012). *Rev. Sci. Instrum.* **83**, 046112.

Nugent, K. A. (2010). *Adv. Phys.* **59**, 1–99.

Quiney, H. M. (2010). *J. Mod. Opt.* **57**, 1109–1149.

Robinson, I. K. & Harder, R. (2009). *Nat. Mater.* **8**, 291–298.

Salome, M., Lafage-Proust, M. H., Vico, L., Amblard, D., Kaulich, B., Oestreich, S., Susini, J, & Barrett, R. (2000). *Am. Inst. Phys. Conf. Proc.* **507**, 178–183.

Schmid, I., Raabe, J., Sarafimov, B., Quitmann, C., Vranjkovic, S., Pellmont, Y. & Hug, H. J. (2010). *Ultramicroscopy*, **110**, 1267–1272.

Schroer, C. G. & Falkenberg, G. (2014). *J. Synchrotron Rad.* **21**, 996–1005.

Schropp, A., Hoppe, R., Patommel, J., Samberg, D., Seiboth, F., Stephan, S., Wellenreuther, G., Falkenberg, G. & Schroer, C. G. (2012). *Appl. Phys. Lett.* **100**, 253112.

Shen, Q., Bazarov, I. & Thibault, P. (2004). *J. Synchrotron Rad.* **11**, 432–438.

Smit, E. de, Swart, I., Creemer, J. F., Groot, F. M. F. de & Weckhuysen, B. M. (2009). *Angew. Chem. Int. Ed.*, **48**, 3632–3636.

Stephan, S. (2013). PhD thesis, TU Dresden, Germany.

Susac, D., Berejnov, V., Hitchcock, A. P. & Stumper, J. (2011). *ECS Trans.* **41**, 629–635.

Susac, D., Berejnov, V., Hitchcock, A. P. & Stumper, J. (2013). *ECS Trans.* **50**, 405–413.

Thibault, P., Dierolf, M., Menzel, A., Bunk, O., David, C. & Pfeiffer, F. (2008). *Science*, **321**, 379–382.

Thibault, P., Guizar-Sicairos, M. & Menzel, A. (2014). *J. Synchrotron Rad.* **21**, 1011–1018.

Thieme, J. (1988). *Proceedings of the 2nd International Conference on X-ray Microscopy* Stony Brook, USA, July 1987. Berlin: Springer-Verlag.

Thieme, J., Sedlmair, J., Gleber, S.-C., Prietzel, J., Coates, J., Eusterhues, K., Abbt-Braun, G. & Salome, M. (2010). *J. Synchrotron Rad.* **17**, 149–157.

Watts, B., Queen, D., Kilcoyne, A. L. D., Tylizsczak, T., Hellman, F. & Ade, H. (2009). *Jpn. J. Appl. Phys.* **186**, 12023.

Withers, P. J. (2007). *Mater. Today*, **10**, 26–34.

Yan, H., Chu, Y. S., Maser, J., Nazaretski, E., Kim, J., Kang, H. C., Lombardo, J. J. & Chiu, W. K. S. (2013). *Nat. Sci. Rep.* **3**, 1307.

Zierod, K. (1988). *J. Electron Microsc. Tech.* **9** 68–82.